ELSEVIER

Contents lists available at ScienceDirect

Organic Electronics

journal homepage: www.elsevier.com/locate/orgel





Efficient and stable perovskite solar cells based on blade-coated CH₃NH₃PbI₃ thin films fabricated using "green" solvents under ambient conditions

Pramod Baral ^a, Xinwen Zhang ^a, Kelsey Garden ^b, Nilave Chakraborty ^b, Lening Shen ^c, Zikun Cao ^a, Xiong Gong ^{c,**}, Luisa Whittaker-Brooks ^{b,***}, He Wang ^{a,*}

ARTICLE INFO

Keywords: Perovskite solar cells Blade coating Ambient condition Green solvent

ABSTRACT

Metal halide perovskites are considered the most promising candidates for solar cells of the decade due to their exceptional optical and electronic properties. The power conversion efficiency of metal halide perovskites, when incorporated as the active layer of solar cells, has become comparable to that observed for conventional silicon solar cells. However, the stability, scaleup, green solvent usage, and fabrication in ambient conditions of metal halide perovskites need to be solved for commercial applications. Here, we report the fabrication of blade-coated methylammonium lead iodide (MAPbI₃) perovskite thin films using methylamine and acetonitrile as "green" solvents under ambient conditions. Our perovskite films are initially prepared from low purity PbI₂ (99%) and are blade-coated in dry air at relative humidity (RH) levels above 30%. A significant advantage of fabricating our perovskite thin films via blade-coating protocols is that there is a minimal amount of precursors (5 μ L) used compared to spin-coating methods (50 μ L -60μ L) for a 4 cm² substrate. With the addition of a small amount of an organic halide salt, namely, phenethylammonium chloride, the film crystallinity is improved and non-radiative recombination is suppressed, resulting in power conversion efficiencies over 20%. In addition, the device maintains more than 95% of its initial efficiency after 500 h under continuous light illumination of 1-sun at open circuit conditions, 50 °C and 60% RH. The above method leads a path towards the commercial fabrication of perovskite solar cells.

1. Introduction

Hybrid metal halide perovskites (MHPs) have attracted extensive attention in both the academic and industry sectors due to their recordbreaking power conversion efficiencies (PCE) of over 25% when incorporated into perovskite solar cells (PSCs) [1]. MHPs possess distinct optoelectronic properties such as high absorption coefficient [2–4], high carrier mobility [5], long carrier diffusion lengths [6,7] and high defect tolerance [8,9], thus leading them as very feasible active components of solar cells, light-emitting diodes, and lasing devices. Through materials engineering [10], controllable crystal growth [11,12], solvent engineering [13–16], anti-solvent engineering [17], surface engineering

[18–20], device engineering [21], etc., efficient and stable PSCs have been reported. However, such significant accomplishments have been reported mostly for small-area PSCs. Moreover, the MHP photoactive layers in these small-area PSC devices have been processed from either a dimethyl formamide (DMF) or a dimethyl sulfoxide (DMSO) precursor solution. Both solvents are not suitable for commercializing large-area panel products. One approach for scaling up PSCs and enabling large-area devices is depositing the MHP photoactive layers using a blade coating method [22–26]. In addition, environmentally friendly solvents are preferred to be used during the fabrication to minimize safety concerns [27]. Compared to commonly used solvents for scaleup (DMF, NMP, etc.), acetonitrile (ACN) [28], which has a lower boiling

E-mail addresses: xgong@uakron.edu (X. Gong), luisa.whittaker@utah.edu (L. Whittaker-Brooks), hewang@miami.edu (H. Wang).

^a Department of Physics, University of Miami, Coral Gables, FL, 33146, USA

^b Department of Chemistry, University of Utah, Salt Lake City, UT, 84112, USA

c School of Polymer Science and Polymer Engineering, College of Engineering and Polymer Science, The University of Akron, Akron, OH, 44325, USA

^{*} Corresponding author.

^{**} Corresponding author.

^{***} Corresponding author.

point in comparison to non-volatile solvents [29,30], is a "green" solvent for making eco-friendly large-area films. For example, Snaith and coworkers have reported using ACN and methylamine as the cosolvent during the fabrication of PSCs. Here, their spin-coating and antisolvent-free fabrication protocol yielded PSCs with PCEs of 19.0% and 16.8% for both conventional and inverted structures, respectively [30]. In another example, Park and coworkers exposed MAPbI₃ powders and crystals to methylamine and dissolved them in an ACN precursor solution. Using a D-bar coating protocol to fabricate films, PCEs up to 17.82% were obtained for PSCs fabricated in a conventional architecture [31].

To achieve efficient PSCs, crystallite orientation and film morphology of the MHP photoactive layer need to be controlled to enhance charge transport. Several methods have been used to tune the crystallization and improve the film quality of the MHP photoactive layer. These methods include composition modulation [32–34], solvent engineering, surface passivation [19,35–37], and additive engineering [38–41]. It turns out that the utilization of process additives is a facile way to control the morphology, nucleation and crystallization of MHP thin films [42,43]. Various studies have demonstrated that halide ions

such as chlorides (with a small radii, 1.67 Å) can fill trap states on the surface or throughout the MHP film. As such, chloride ions have been used as process additives [44] to tune the film morphology of MHP, resulting in efficient and stable PSCs [45].

In this study, we report efficient and stable PSCs based on bladecoated CH3NH3PbI3 (MAPbI3) thin films fabricated using "green" solvents with the addition of phenethylammonium chloride (PEACl) in ambient conditions. We prepare MAPbI₃ powders and single crystal thin films from ACN as the "green" solvent rather than using either DMF or DMSO solvents. Upon blade coating our films over a 2 cm \times 2 cm substrate, we minimize the amount of precursors (5 μ L) used in comparison to spin coating (50µL-60 µL) in ambient conditions with relative humidity (RH) levels above 30%. To further tune the film morphology of the MHP photoactive layer, PEACl, as a processing additive, is mixed with the MAPbI₃ precursor solution. Interestingly, we found that only a small amount of additive significantly tunes the film morphology and valence band maximum, resulting in enhanced PCEs over 20%. We observe that the PSCs based on MAPbI₃ with PEACl as the processing additive maintain more than 95% of their initial PCEs under white light illumination continuously for 500 h under open-circuit condition in air

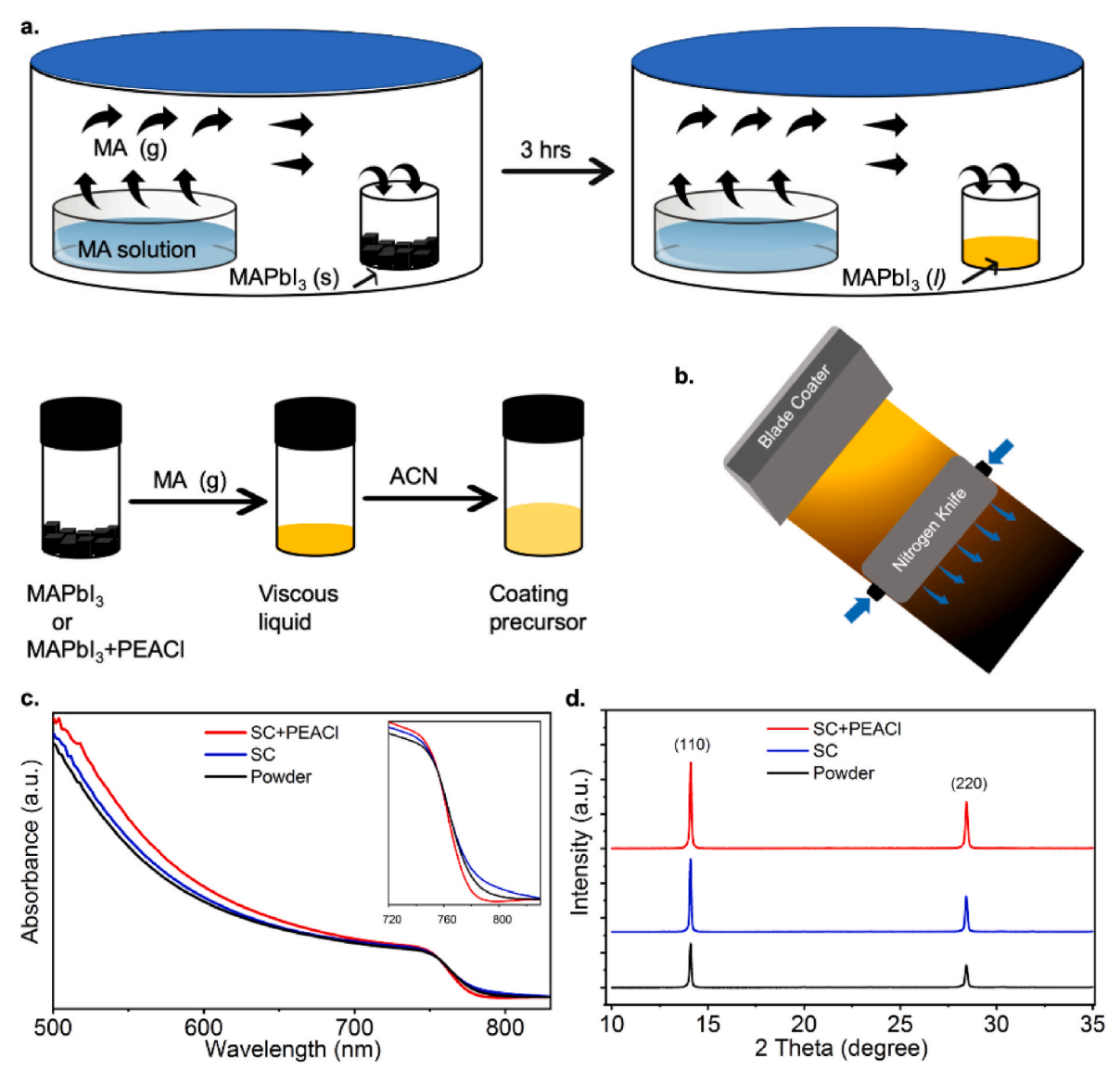


Fig. 1. (a) Schematic illustration showing the preparation procedure of the coating precursor using volatile solvents (methylamine + ACN). (b) Schematic diagram of the blade coater and the nitrogen knife used to fabricate a dark-uniform MHP film. (c) UV–Vis absorption spectra of three different MHP films fabricated with powder MAPbI₃, MAPbI₃ single crystals, and PEACl mixed with MAPbI₃ single crystals. (d) XRD patterns of the three different films.

at 50 °C and 60% RH.

2. Experimental section

Materials: Indium tin oxide (ITO) was purchased from Advanced Election Technology Co., Ltd. C_{60} (99%) was purchased from Nano-C. 1-Propanol was purchased from Fisher Chemical. Diethyl-ether was purchased from TCI America. Methylammonium iodide (MAI) and PEACl were purchased from Greatcell Solar. Lead (II) iodide (PbI₂) (99%), poly [bis(4-phenyl)(2,4,6-trimethylphenyl)amine] (PTAA), methylamine solution (33 wt% in absolute ethanol), bathocuproine (BCP) (99.99%) and all other solvents (anhydrous, \geq 99.8%) were purchased from Millipore Sigma. All materials are used as received without further purification.

MAPbI₃ **Powder:** 3.6 mmol (0.5724 g) of MAI was dissolved in 12 mL ACN under continuous stirring. Subsequently, 3 mmol of PbI₂ (1.383 g) was slowly mixed with the above solution and stirred overnight. This process yields a black MAPbI₃ powder that was then washed 6–8 times using ACN and diethyl-ether, separately. The washed black powder was put under vacuum for 12 h, and then dried at 70 °C for 24 h.

 $MAPbI_3$ Single Crystals (SC): Single crystals were grown using the inverse temperature crystallization (ITC) method [46]. Both 1 M MAI and 1 M PbI $_2$ were completely dissolved into 2 mL GBL solvent in a small vial which was then filtered and put in an oil bath at 110 $^{\circ}\text{C}$. MAPbI $_3$ single crystals were collected after 10 h and then washed a few times using propanol.

Perovskite Thin Film Characterization: XRD measurements were performed using a PANalytical X-ray diffractometer with a step size of 0.01°. UV-Visible linear absorption spectroscopy was measured using an Agilent UV spectrophotometer (Cary 60). A Horiba fluorescence instrument was used to measure steady-state photoluminescence (PL) and time-resolved PL. Transient absorption (TA) measurements were carried out using a Ti:sapphire laser (800 nm) at a repetition rate of 5 kHz (Coherent Astrella). A 400 nm pump pulse was generated using an optical parametric amplifier (OPA), while a probe pulse of supercontinuum white light was generated by focusing a small portion of fundamental laser onto a sapphire. The pump-probe pulses were aligned to focus on a single point of the sample with a cross-correlation of ~100 femtosecond (fs) and the TA spectra were collected on a commercial pump-probe spectrometer (Helios Fire, Ultrafast Systems). A solar cell quantum efficiency measurement system (QEX10) with a 300 W steady-state xenon lamp as a source light was used to measure the external quantum efficiency (EQE). X-ray photoelectron spectroscopy (XPS) data were extracted from a Kratos Axis Ultra DLD. Ultraviolet photoelectron spectroscopy (UPS) data were recorded using a Kratos Axis Ultra DLD with a He I line at 21.22 eV. Scanning electron microscopy (SEM) images were collected using a field-emission gun (FEI Quanta 600F). Atomic force microscopy (AFM) images were collected using a Bruker dimension icon atomic force microscope in tapping mode.

PSC Fabrication: Patterned ITO substrates were cleaned sequentially with detergent, deionized water, isopropanol, and acetone for 15 min each using an ultrasonicator. The ITO substrates were dried inside an oven at 60 $^{\circ}$ C. The substrates were treated with UV ozone for 15 min to clean the surface before depositing the PTAA as a hole transport layer. After transferring the cleaned ITO substrates to the glovebox, a PTAA thin film was spin coated (2 mg/mL in toluene) at 500 rpm for 5 s and then at 4500 rpm for another 30 s. The PTAA coated substrates were then annealed at 100 °C for 10 min, and then cooled down to room temperature naturally. Afterwards, a 150 µL DMF was spincoated on top of the PTAA thin layer to make its surface wet and hydrophilic. For the pristine MHP precursor, 100 mg MAPbI₃ powder or single crystal was placed in a lid-open vial inside a fully closed 1L container. The MHP precursor was then reacted with methylamine gas produced from a 2 mL methylamine solution for 3 h. A viscous liquid was obtained that was then diluted with ACN with a weight ratio of 60:40. For PEACl added MHP precursor, a 1% molar ratio relative to MAPbI₃ was mixed with the single crystals in a lid open vial before exposing it to methylamine gas. 5

 μL of ACN diluted viscous liquid was blade coated over the PTAA spin coated ITO substrate (2 cm \times 2 cm) using a blade coater in dry air at RH \sim 30% and a nitrogen knife at a pressure lower than 5 psi was used to evaporate the solvent. A dark and uniform MHP film was then created. The gap between the blade coater and the substrate was tuned to 150 μm and the blade coating speed was 3.5 mm/s. All blade-coated films were annealed at 110 °C for 10 min at RH levels between 30% and 50%. Subsequently, 30 nm C60 and 10 nm BCP were sequentially thermally evaporated in a vacuum with a base pressure of 1.5 \times 10 $^{-6}$ Torr. Finally, 90 nm copper was thermally evaporated as a top electrode with an active area of 0.1 cm² for each cell.

PSC Characterization and Photostability Test: The current density versus voltage (*J-V*) curves and stabilized PCE of encapsulated PSCs were measured using a Keithley source meter (2612B) under AM 1.5G 100 mW/cm² illumination with a Xenon solar simulator. Photostability test was carried out using a white light-emitting diode (LED) lamp at 100 mW/cm², 60% RH, and 50 °C. The encapsulation process was carried out under vacuum and at a temperature of 120 °C for 5 min. Edge encapsulation was carried out using desiccated butyl/polyisobutylene (PIB) (Quanex SET LP03) only at the edge between the device and a transparent glass piece. Covered encapsulation was done over the entire device, leaving no gap between the cell and the cover glass.

3. Results and discussion

Fig. 1a illustrates the preparation procedure of the blade coating method at room temperature. The $MAPbI_3$ powder or single-crystal (SC) or PEACl-incorporated $MAPbI_3$ SC was put in a small vial, and then it was placed together with a Petri dish containing a methylamine solution in a closed container. The solid $MAPbI_3$ changed to a yellowish viscous liquid upon exposure to a methylamine vapor produced from a methylamine solution. ACN solution was added to this viscous, yellowish liquid to get a blade-coated precursor.

Fig. 1b displays the schematic diagram of a blade coater and nitrogen knife used to prepare MHP films. A speed of 3.5 mm/s and air-knife pressure of <5 psi was used while blade coating to get uniform and highly crystalline films. The mixture of two volatile solvents methylamine/ACN plays a vital role in controlling the nucleation, crystallization, and crystal growth processes during the blade-coating process. A compact and uniform MHP film was formed after the blade coating, as shown in Fig. S1 (AFM images) and Table S1 (AFM roughness). We studied the composition of MAI and PbI₂ during the preparation of the MAPbI₃ powder. We tried three different MAI:PbI₂ molar ratio and found that a 1.2:1 ratio works best given that it yields the highest absorption and photoluminescence signals, as shown in Fig. S2, and therefore this ratio is selected in this work.

Fig. 1c shows the ultraviolet-visible (UV-Vis) absorption spectra of MAPbI3 thin films cast from MAPbI3 powder, MAPbI3 SC and PEAClincorporated MAPbI₃ SC. They all display similar shapes, except for the sharpness of the band-edge. The MHP film made using the SC with the PEACl additive exhibits a sharper bandgap, which probably originates from better film quality, such as crystallinity. Fig. 1d displays the X-ray diffraction (XRD) patterns for these three different MAPbI₃ thin films. The peaks at 14.11° and 28.42°, which correspond to the (110) and (220) planes, respectively, are presented in these three thin films, indicating that they all possess a tetragonal crystal structure. However, compared to the MAPbI₃-powder thin film, the MAPbI₃-SC thin film shows a higher peak intensity (increased by 67%) of the (110) plane, which indicates that the MAPbI₃-SC thin film exhibits superior crystallinity compared to the MAPbI3-powder thin film. Moreover, the peak intensity value observed from the 1% PEACl-incorporated MAPbI3-SC thin film is also slightly increased (increased by 18.8%) compared with the MAPbI₃-SC thin film, suggesting that the 1% PEACl-incorporated MAPbI₃-SC thin film possesses higher crystallinity. This composition is also selected based on our device optimization. Fig. S3 displays the J-Vcharacteristics of devices with different amounts of PEACl, and we found

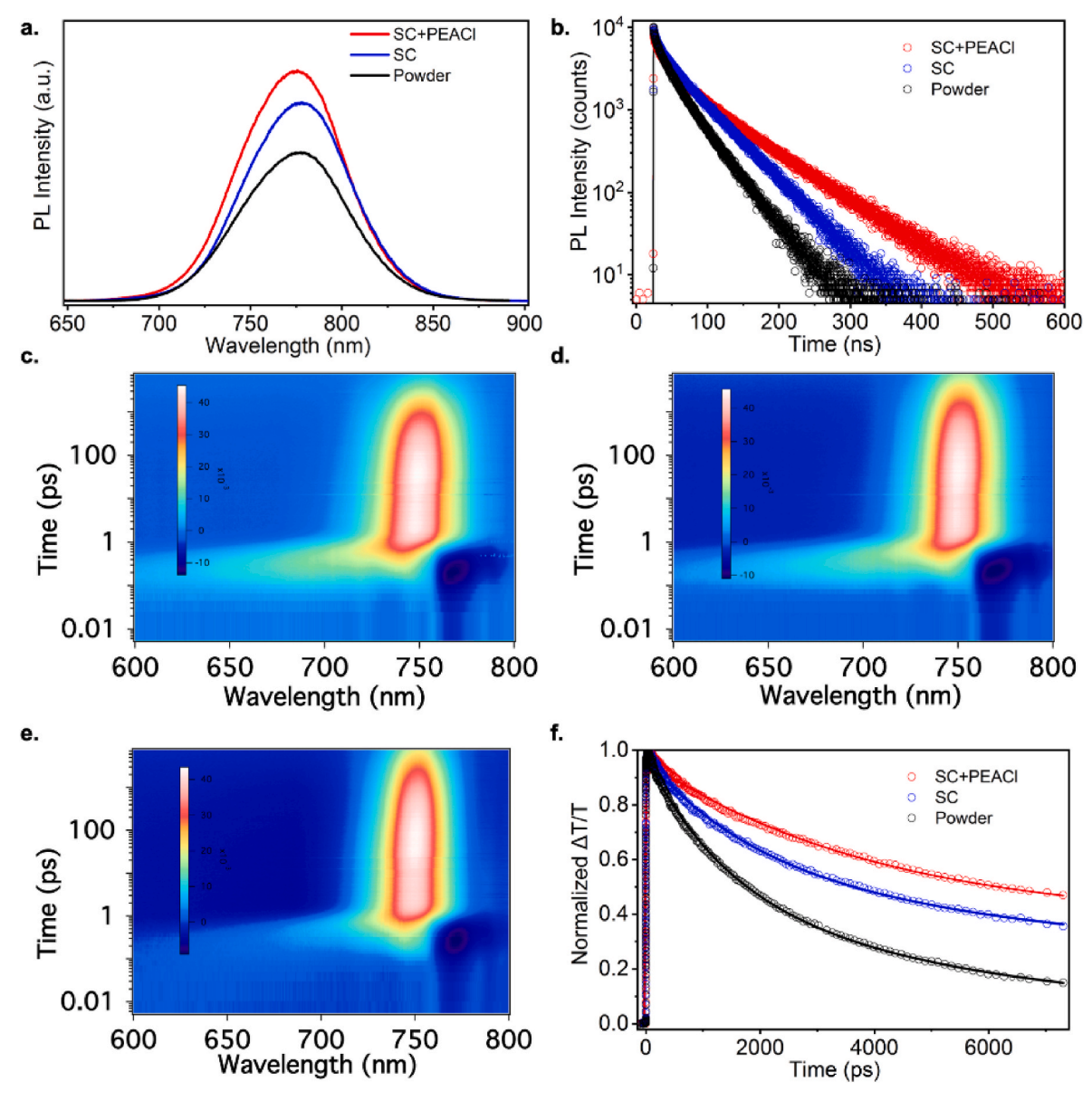


Fig. 2. (a) Steady-state PL spectra for three different MHP films made by MAPbI₃ powder, SC, and SC + PEACl. (b) PL decay curves for these films. Transient absorption maps of the three different MHP films made by (c) powder, (d) SC, and (e) SC + PEACl, obtained from femtosecond-laser spectroscopy. (f) Decay kinetics at 751 nm observed in all three cases.

that 1% PEACl yields the highest PSC efficiencies.

To reveal the quality of the prepared films and charge carrier dynamics, steady-state photoluminescence (PL) and time-resolved PL (TRPL) experiments were performed with an excitation wavelength of 405 nm. Fig. 2a shows the PL spectra of MAPbI₃ thin films. We observed that the thin films obtained from the PEACl-incorporated MAPbI₃ SC show the strongest PL peak intensity suggesting that defects within these films are reduced. Fig. 2b shows the TRPL for powder, SC, and PEAClincorporated MAPbI3 SC thin films. The PL lifetime for all the films are fitted using a bi-exponential equation. The longer lifetime indicates that the surface or bulk possesses fewer defect states. The fitting gives τ_1 = 2.03 ns (weight ratio of 3%) and τ_2 = 26.08 ns (weight ratio of 97%) for films prepared from the MAPbI₃ powder. The lifetime is increased to $\tau_1 = 2.56$ ns (weight ratio of 3%) and $\tau_2 = 36.97$ ns (weight ratio of 97%) for a sample made from a MAPbI₃ SC. After the incorporation of PEACl, the lifetime is further increased to $\tau_1 = 7.85$ ns (weight ratio of 10%) and $\tau_2 = 57.51$ ns (weight ratio of 90%). Decay curves from the TRPL measurement enlightened the fact that PEACl helps on reducing defect density and associated non-radiative recombination, thus enhancing charge carrier lifetime.

To better understand the charge carrier dynamics in the shorter time scale, i.e. to study the ultrafast recombination process, transient absorption (TA) measurements were performed. Fig. 2c-e represents the TA spectra obtained from femtosecond-laser spectroscopy for the three different types of MAPbI3 samples. While collecting data, a 400 nm pump laser comprising a power of 10 μJ/cm² was used to excite the MAPbI₃ films. Two types of signals appeared in our graphs: a positive signal representing ground state bleaching along with stimulated emission, and a negative signal representing excited state absorption [47]. Fig. 2f represents the kinetics extracted for the different films at a wavelength of 751 nm, demonstrating that the lifetime for the PEACl-incorporated MAPbI₃ SC thin films is higher. The TA kinetics are fitted using a bi-exponential Gaussian function with τ_1 and τ_2 featuring faster and slower decay time components. The fast decay component corresponds to the trap-assisted recombination process at grain boundaries, while the slower decay component corresponds to the radiative

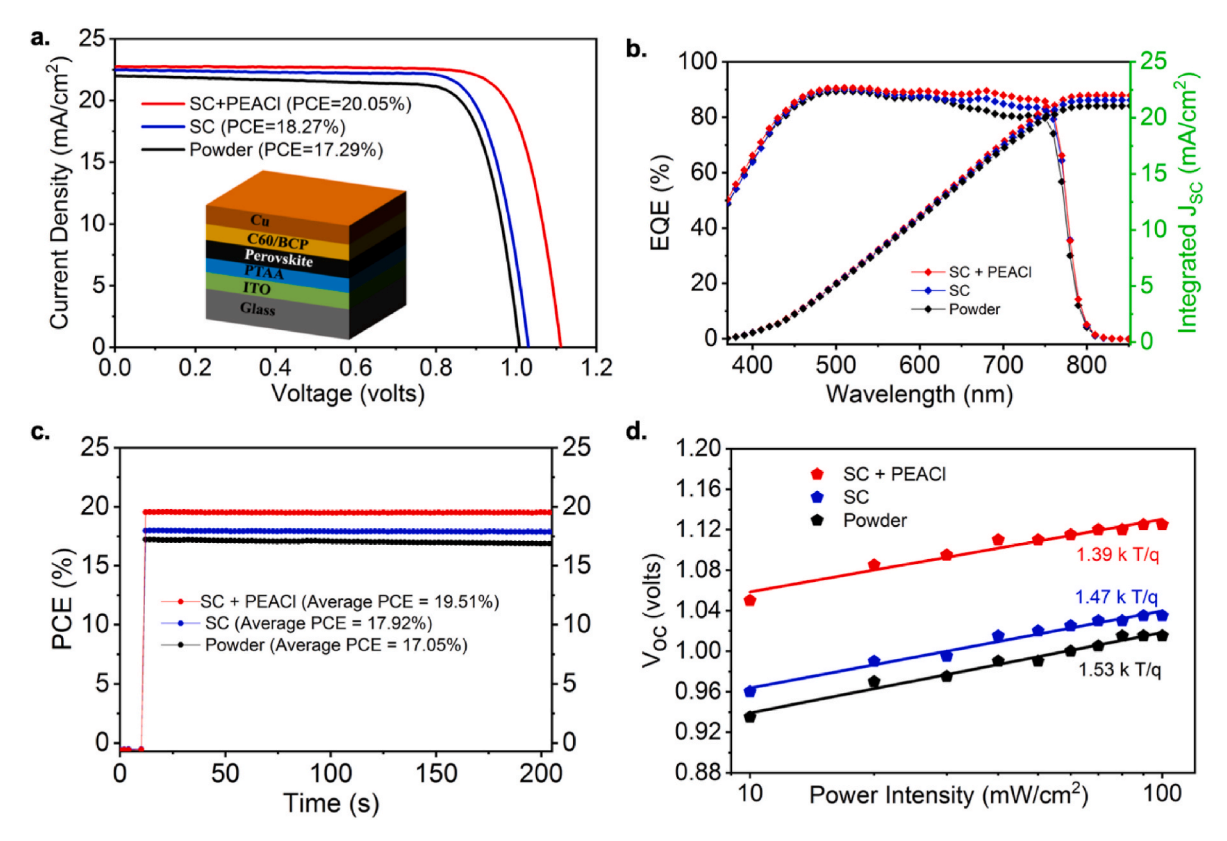


Fig. 3. (a) J-V curves extracted from devices made with MAPbI₃ powder, SC, and PEACl mixed SC. (Inset represents the schematic representation of a p-i-n inverted device structure showing different layers.) (b) EQE curves for all three samples. (c) Stabilized PCE lines from all three samples recorded for 200 s. (d) Semi-log plot showing the V_{OC} dependence on light intensities.

recombination process inside the grains [48]. The fitting gives $\tau_1=0.79$ ns (weight ratio of 54%) and $\tau_2=3.09$ ns (weight ratio of 46%) for the powder sample. The lifetime is increased to $\tau_1=1.00$ ns (weight ratio of 48%) and $\tau_2=10.67$ ns (weight ratio of 52%) for a thin film sample made from a single crystal. After the incorporation of PEACl, the lifetime is further increased to $\tau_1=2.76$ ns (weight ratio of 65%) and $\tau_2=49.30$ ns (weight ratio of 35%). This result is consistent with our steady-state and time-resolved PL measurements, as well as the XRD results. Overall, the MHP films made from single crystals are better than that made from powders. The incorporation of PEACl within the MAPbI $_3$ thin film exhibits the best film quality and photophysical responses.

Fig. 3a shows the J-V curves of the PSCs based on either MAPbI₃powder or MAPbI₃-SC or MAPbI₃-SC W/PEACl thin films. Inset in Fig. 3a displays the schematic representation of the p-i-n device structure ITO/ PTAA/perovskite/C₆₀/BCP/Cu, where PTAA (hole transport layer) is prepared by spin coating, the MHP layer is deposited by blade coating, C₆₀/BCP (electron transport layer) and Cu electrode are thermally evaporated. The PSCs based on the MAPbI3-powder thin film exhibit a short-circuit current density (J_{SC}) of 22.00 mA/cm², an open-circuit voltage (V_{OC}) of 1.01 V, a fill factor (FF) of 0.78, resulting in a PCE of 17.29%. The PSCs based on the MAPbI $_3$ -SC exhibit a J $_{SC}$ of 22.47 mA/ $\rm cm^2$, a $\rm V_{OC}$ of 1.03 V, a FF of 0.79, resulting in a PCE of 18.27%. The PSCs based on the MAPbI $_3$ -SC W/PEACl have a J $_{SC}$ of 22.75 mA/cm 2 , a V $_{OC}$ of 1.11 V, FF of 0.80, resulting in a PCE of 20.05%. This enhancement in device performance after adding PEACl, mainly due to improved VOC, is consistent with its higher crystallinity and longer carrier lifetime. Fig. 3b displays the external quantum efficiency (EQE) and integrated J_{SC} of PSCs prepared with powder, SC, and PEACl mixed with SC. The integrated J_{SC} values are 21.06 mA/cm², 21.59 mA/cm², and 22.02 mA/cm² respectively which are consistent with those obtained from the J-V curves. Fig. 3c represents the stabilized PCE curves for 200 s. Devices fabricated with powder and SC of MAPbI3 have an average PCE of 17.05% and 17.92% at maximum point biasing voltage of 0.875 V and 0.890 V, respectively. The PSC devices fabricated upon the addition of PEACl show an average PCE of 19.51% while using the maximum power point biasing voltage of 0.935 V. Device response studies under different light intensities ranging from 10 mW/cm² to 100 mW/cm² were also carried out and it is found that all three types of devices show a linear J_{SC} versus light intensity relationship (Fig. S4). This implies that even though the insulating molecule PEACl is introduced within the MHP layer, there is no obvious charge barrier induced at the interface [19]. The light intensity-dependent V_{OC} plots are displayed in Fig. 3d. Here, the slope of these linearly fitted graphs gives us insights into the recombination mechanism. For $MAPbI_3$ powder and SC, the slope is 1.53 kT/q and 1.47 kT/q, respectively, where 'k' is the Boltzmann constant, 'T' is the absolute temperature and 'q' is the basic charge. In the presence of PEACl, the slope is 1.39 kT/q. The smaller slope indicates that the PEACl-incorporated PSCs exhibit suppressed trap-assisted recombination as compared to the powder and SC MAPbI3 films, resulting in a boosted PCE.

To better understand the surface morphology and energy band alignment for our MHP films, we carried out the characterization using different techniques such as SEM, XPS, and UPS. Fig. 4a–c displays the SEM images for thin films blade coated using precursors made with MAPbI₃ powder, MAPbI₃ SCs, and PEACl added into SCs. From the SEM images, we can infer that the MHP film fabricated from SC exhibits slightly larger grain sizes than that made from MAPbI₃ powder. The addition of PEACl significantly affects the film morphology. The incorporation of PEACl within the MAPbI₃ film decreases grain sizes but passivates the grain boundaries. Given that the device performance is improved with PEACl, it suggests the grain size is less significant than the passivation of grain boundaries. Moreover, we know that a photon with a longer wavelength can penetrate deeper into the sample, thus, the surface morphology influenced by PEACl is consistent with the higher

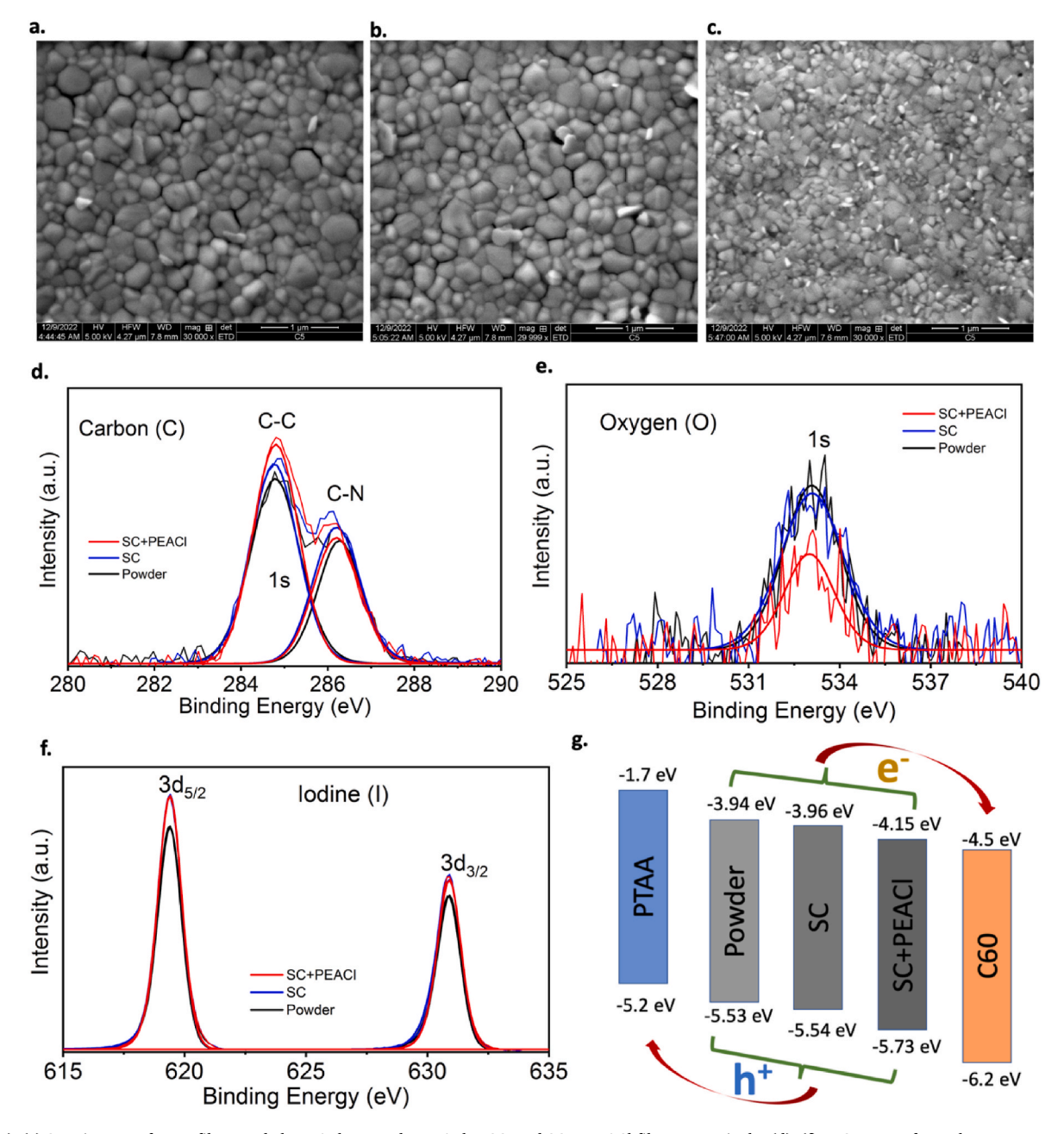


Fig. 4. (a)–(c) SEM images of MHP films made by MAPbI $_3$ powder, MAPbI $_3$ SC, and SC + PEACl film, respectively. (d)–(f) XPS spectra for carbon, oxygen, and iodine present in the three films, respectively. (g) Energy level alignment diagram for all three sample films based on UPS results, along with the ETL (C60) and HTL (PTAA) layers.

intensity observed for the EQE at longer wavelengths (Fig. 3b). To qualitatively determine the elemental compositions on our thin films, we also performed XPS which is sensitive to the compositions of films on the top few nanometers. Fig. S5 shows the XPS spectra for lead (4f $_{5/2}$ and 4f $_{7/2}$ state), for which all our films behave similarly. Fig. 4d–f shows the XPS spectra for the carbon, oxygen, and iodine edges. There are two peaks for carbon in Fig. 4d at a binding energy of 286.5 eV which has been attributed to C–N bond, and a peak at 284.8 eV which has been attributed to C–C bonds [49]. The PEACl added sample giving a stronger peak at 284.8 eV suggests that more C–C bonds are present on the top few nanometers coming from PEACl aggregating at the surface. Fig. 4e represents the XPS data for oxygen having peaks at 533 eV and shows that a lower amount of oxygen is present on the surface of the film containing PEACl, which in turn suggests the formation of more environmentally stable films as these are not oxidized. This finding is again

corroborated by our photostability tests that shows that the PEACl-incorporated PSC devices in ambient conditions are more stable and efficient. Fig. 4f shows the XPS spectra for the iodine edge (3d states), for which the powder sample exhibits a slightly lower intensity. We also performed the UPS to test the energy alignment on the top surface of three comparing films. Plotted curves for our samples highlighting the work function (Φ) and valence band maximum (VBM) energy level are shown in the supporting information (Figs. S6–S8). Given the bandgap (extracted from EQE) measured for the three comparing films (powder 1.59 eV, single crystal 1.58 eV, and single crystal + PEACl 1.58 eV), we plot the energy band level as shown in Fig. 4g. No big difference is noticed in the valence band maximum from powder and single crystal films. However, the single crystal with PEACl film gives a distinctly higher value, which suggests that undesired hole transport may be blocked from the MHP to C60 in a more effective manner. The

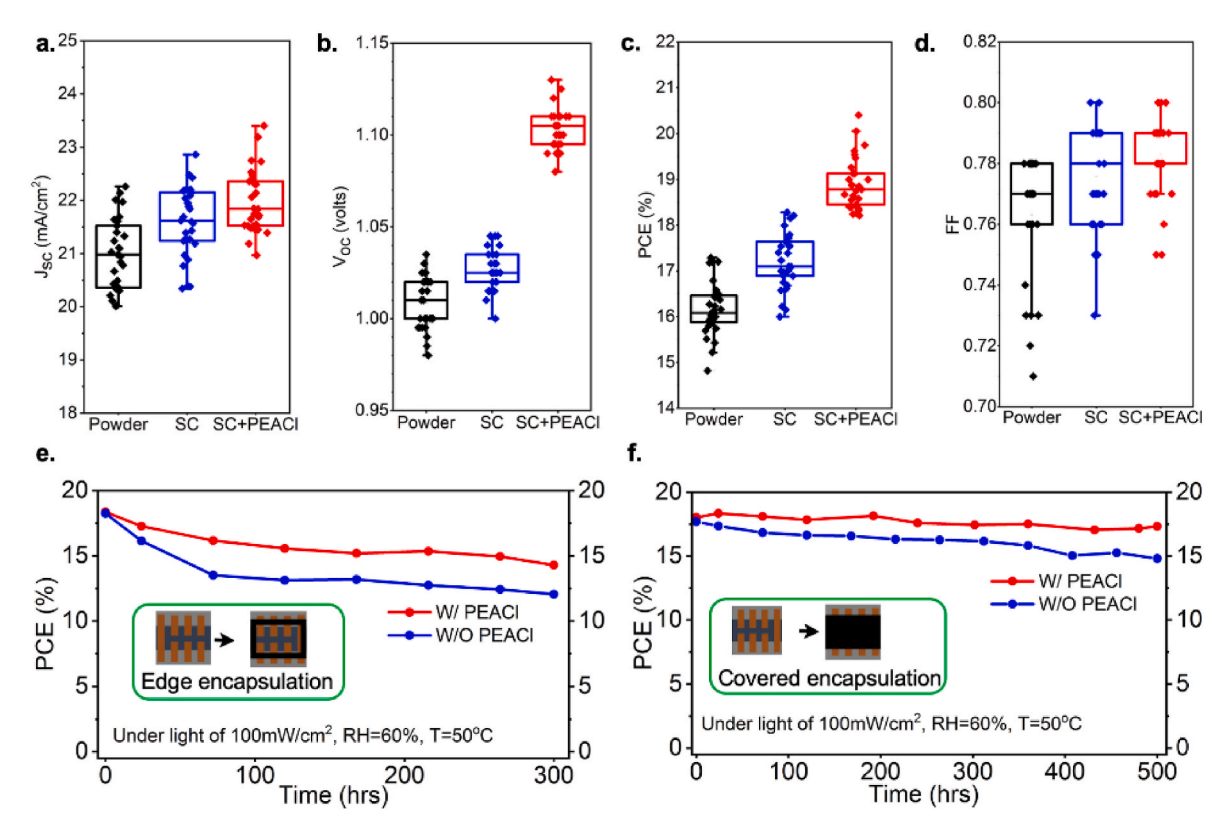


Fig. 5. (a)–(d) Box and whisker plot showing statistical distributions of J_{SC} , V_{OC} , PCE, and FF from devices prepared with three types of MHP films. (e) Photostability curves with edge encapsulation for MAPbI₃ SC and SC + PEACl samples. (f) Photostability curves with covered encapsulation for SC and SC + PEACl films.

lower conduction band value from our optimized MHP reduces the conduction band energy offset between the MHP and C60, giving us a more efficient path for electron transport and thus more efficient devices.

Fig. 5a-d represents the statistical distributions of photovoltaic parameters for 30 cells from each MAPbI3 thin films using a box and whisker plot. For the powder case, the average photovoltaic parameters J_{SC}, V_{OC}, PCE, FF are 21.00 mA/cm², 1.01 V, 16.16%, 0.763, respectively. The average photovoltaic parameters J_{SC}, V_{OC}, PCE, FF using MAPbI₃ SC are 21.60 mA/cm², 1.03 V, 17.21%, 0.776, respectively, whereas from the PEACl added precursor, we got those parameters as 21.98 mA/cm², 1.10 V, 18.90%, 0.783, respectively. Fig. 5e shows the photostability curve comparison of devices with edge encapsulation, fabricated using MAPbI3 precursors from SC and PEACl. The photostability curves show that the PEACl-incorporated PSC devices are more stable under continuous white light illumination of 1-sun at 50 °C and 60% RH. All the encapsulations are done using a vacuum sealing method, where the encapsulant is put in between the device and the transparent glass. Fig. 5f shows the photostability curve using the covered encapsulation method for pristine MAPbI3 and PEACl added PSC devices. The photostability test performance provided more insights into the role of PEACl in MAPbI₃ films. Using the covered encapsulation technique, as explained in the experimental section, we observe that the PEACI-PSC device performance is improved in comparison to the pristine one. We also observe that the stability over more than 500 h of constant illumination under open-circuit condition at 50 $^{\circ}$ C and 60% RH is significantly improved upon the addition of PEACl to the MAPbI₃ film. As shown in Fig. 5e-f, more than 95% of the initial PSC efficiency is maintained when PEACl is added to MAPbI3, while for the pristine device less than 85% on its performance is mantained.

4. Conclusion

In summary, we found that using a small amount of PEACl as an

additive leads to better crystallinity and fewer defects in MHP films. Our devices fabricated using precursors cast from volatile and green solvents (methylamine/ACN) and blade coated in air at RH levels above 30% show PCE values above 20%. More importantly, our devices maintained more than 95% of their initial PCEs after continuous white light illumination of 1-sun for 500 h under open circuit condition at 50 °C and 60% RH. This work provides a pathway for fabricating large area devices with efficient and stable performances, and also a gateway for the fabrication of PSC devices from green solvents.

Author contributions

The manuscript was written through contributions of all authors. All authors have given approval to the final version of the manuscript.

Declaration of competing interest

The authors declare that they have no known competing financial interests or personal relationships that could have appeared to influence the work reported in this paper.

Data availability

Data will be made available on request.

Acknowledgments

H. W. acknowledges the financial support by the Air Force Office of Scientific Research (AFOSR) under award number FA9550-17-1-0099 and FA9550-21-1-0192. LWB would like to acknowledge support from the U.S. Department of Energy, Office of Basic Energy Sciences, Division of Materials Sciences and Engineering under Award no. DE-SC0019041. X. G. acknowledges the financial support from the National Science Foundation (NSF) (ECCS/EPMD1903303) and the AFOSR (through the

Organic Materials Chemistry Program, Grant Number: FA9550-15-1-0292, Program Manager, Dr. Kenneth Caster).

Appendix A. Supplementary data

Supplementary data to this article can be found online at https://doi.org/10.1016/j.orgel.2023.106763.

References

- [1] M. Kim, J. Jeong, H. Lu, T.K. Lee, F.T. Eickemeyer, Y. Liu, I.W. Choi, S.J. Choi, Y. Jo, H.B. Kim, Conformal quantum dot–SnO2 layers as electron transporters for efficient perovskite solar cells, Science 375 (2022) 302–306, https://doi.org/ 10.1126/science.abh1885.
- [2] A.M. Leguy, P. Azarhoosh, M.I. Alonso, M. Campoy-Quiles, O.J. Weber, J. Yao, D. Bryant, M.T. Weller, J. Nelson, A. Walsh, Experimental and theoretical optical properties of methylammonium lead halide perovskites, Nanoscale 8 (2016) 6317–6327, https://doi.org/10.1039/CSNR05435D.
- [3] S. De Wolf, J. Holovsky, S.J. Moon, P. Loper, B. Niesen, M. Ledinsky, F.J. Haug, J. H. Yum, C. Ballif, Organometallic halide perovskites: sharp optical absorption edge and its relation to photovoltaic performance, J. Phys. Chem. Lett. 5 (2014) 1035–1039, https://doi.org/10.1021/jz500279b.
- [4] J. Qian, B. Xu, W. Tian, A comprehensive theoretical study of halide perovskites ABX₃, Org. Electron. 37 (2016) 61–73, https://doi.org/10.1016/j. orgel.2016.05.046.
- [5] J. Lim, M.T. Hörantner, N. Sakai, J.M. Ball, S. Mahesh, N.K. Noel, Y.H. Lin, J. B. Patel, D.P. McMeekin, M.B. Johnston, Elucidating the long-range charge carrier mobility in metal halide perovskite thin films, Energy Environ. Sci. 12 (2019) 169–176, https://doi.org/10.1039/C8EE03395A.
- [6] S.D. Stranks, G.E. Eperon, G. Grancini, C. Menelaou, M.J. Alcocer, T. Leijtens, L. M. Herz, A. Petrozza, H.J. Snaith, Electron-hole diffusion lengths exceeding 1 micrometer in an organometal trihalide perovskite absorber, Science 342 (2013) 341–344, https://doi.org/10.1126/science.1243982.
- [7] C. Zuo, H.J. Bolink, H. Han, J. Huang, D. Cahen, L. Ding, Advances in perovskite solar cells, Adv. Sci. 3 (2016), 1500324, https://doi.org/10.1002/ advs. 2015.00324
- [8] H. Huang, M.I. Bodnarchuk, S.V. Kershaw, M.V. Kovalenko, A.L. Rogach, Lead halide perovskite nanocrystals in the research spotlight: stability and defect tolerance, ACS Energy Lett. 2 (2017) 2071–2083, https://doi.org/10.1021/ acsenersylett.7b00547.
- [9] W. Chu, Q. Zheng, O.V. Prezhdo, J. Zhao, W.A. Saidi, Low-frequency lattice phonons in halide perovskites explain high defect tolerance toward electron-hole recombination, Sci. Adv. 6 (2020), eaaw7453, https://doi.org/10.1126/sciadv. aaw7453
- [10] M. Morana, L. Malavasi, Pressure effects on lead-free metal halide perovskites: a route to design optimized materials for photovoltaics, Solar RRL 5 (2021), 2100550, https://doi.org/10.1002/solr.202100550.
- [11] C. Liu, Y.B. Cheng, Z. Ge, Understanding of perovskite crystal growth and film formation in scalable deposition processes, Chem. Soc. Rev. 49 (2020) 1653–1687, https://doi.org/10.1039/C9CS00711C.
- [12] Z. Chen, B. Turedi, A.Y. Alsalloum, C. Yang, X. Zheng, I. Gereige, A. AlSaggaf, O. F. Mohammed, O.M. Bakr, Single-crystal MAPbI₃ perovskite solar cells exceeding 21% power conversion efficiency, ACS Energy Lett. 4 (2019) 1258–1259, https://doi.org/10.1021/acsenergylett.9b00847.
- [13] N.J. Jeon, J.H. Noh, Y.C. Kim, W.S. Yang, S. Ryu, S.I. Seok, Solvent engineering for high-performance inorganic-organic hybrid perovskite solar cells, Nat. Mater. 13 (2014) 897–903, https://doi.org/10.1038/nmat4014.
- [14] Y. Rong, Z. Tang, Y. Zhao, X. Zhong, S. Venkatesan, H. Graham, M. Patton, Y. Jing, A.M. Guloy, Y. Yao, Solvent engineering towards controlled grain growth in perovskite planar heterojunction solar cells, Nanoscale 7 (2015) 10595–10599, https://doi.org/10.1039/C5NR02866C.
- [15] Z. Arain, C. Liu, Y. Yang, M. Mateen, Y. Ren, Y. Ding, X. Liu, Z. Ali, M. Kumar, S. Dai, Elucidating the dynamics of solvent engineering for perovskite solar cells, Sci. China Mater. 62 (2019) 161–172, https://doi.org/10.1007/s40843-018-9336-1
- [16] A.S. Subbiah, F.H. Isikgor, C.T. Howells, M. De Bastiani, J. Liu, E. Aydin, F. Furlan, T.G. Allen, F. Xu, S. Zhumagali, S. Hoogland, E.H. Sargent, I. McCulloch, S. De Wolf, High-performance perovskite single-junction and textured perovskite/silicon tandem solar cells via slot-die-coating, ACS Energy Lett. 5 (2020) 3034–3040, https://doi.org/10.1021/acsenergylett.0c01297.
- [17] S.M. Majeed, D.S. Ahmed, M.K.A. Mohammed, Anti-solvent engineering via potassium bromide additive for highly efficient and stable perovskite solar cells, Org. Electron. 99 (2021), 106310, https://doi.org/10.1016/j.orgel.2021.106310.
- [18] J.F. Wang, L. Zhu, B.G. Zhao, Y.L. Zhao, J. Song, X.Q. Gu, Y.H. Qiang, Surface engineering of perovskite films for efficient solar cells, Sci. Rep. 7 (2017) 1–9, https://doi.org/10.1038/s41598-017-14920-w.
- [19] Q. Jiang, Y. Zhao, X. Zhang, X. Yang, Y. Chen, Z. Chu, Q. Ye, X. Li, Z. Yin, J. You, Surface passivation of perovskite film for efficient solar cells, Nat. Photonics 13 (2019) 460–466. https://doi.org/10.1038/s41566-019-0398-2.
- [20] B. Li, Y. Zhang, L. Fu, T. Yu, S. Zhou, L. Zhang, L. Yin, Surface passivation engineering strategy to fully-inorganic cubic CsPbI₃ perovskites for highperformance solar cells, Nat. Commun. 9 (2018) 1–8, https://doi.org/10.1038/ s41467-018-03169-0.

- [21] L. Meng, J. You, Y. Yang, Addressing the stability issue of perovskite solar cells for commercial applications, Nat. Commun. 9 (2018) 5265, https://doi.org/10.1038/ s41467-018-07255-1.
- [22] S. Razza, F. Di Giacomo, F. Matteocci, L. Cina, A.L. Palma, S. Casaluci, P. Cameron, A. D'epifanio, S. Licoccia, A. Reale, Perovskite solar cells and large area modules (100 cm²) based on an air flow-assisted PbI₂ blade coating deposition process, J. Power Sources 277 (2015) 286–291, https://doi.org/10.1016/j.jpowsour.2014.12.008.
- [23] C. Li, J. Yin, R. Chen, X. Lv, X. Feng, Y. Wu, J. Cao, Monoammonium porphyrin for blade-coating stable large-area perovskite solar cells with> 18% efficiency, J. Am. Chem. Soc. 141 (2019) 6345–6351, https://doi.org/10.1021/jacs.9b01305.
- [24] Y. Xiao, C. Zuo, J.X. Zhong, W.Q. Wu, L. Shen, L. Ding, Large-area blade-coated solar cells: advances and perspectives, Adv. Energy Mater. 11 (2021), 2100378, https://doi.org/10.1002/aenm.202100378.
- [25] Y. Peng, F. Zeng, Y. Cheng, C. Wang, K. Huang, P. Xie, H. Xie, Y. Gao, J. Yang, Fully Doctor-bladed efficient perovskite solar cells in ambient condition via composition engineering, Org. Electron. 83 (2020), 105736, https://doi.org/10.1016/j. orgel.2020.105736.
- [26] X. Zhang, P. Baral, N. Chakraborty, K. Garden, L. Shen, S.N. Vijayaraghavan, Z. Cao, F. Yan, X. Gong, L. Whittaker-Brooks, H. Wang, Blade coating inverted perovskite solar cells with vacuum assisted nucleation based on bottom quasi-2D passivation, Solar RRL (2023), 2200900, https://doi.org/10.1002/ solr.202200900.
- [27] N.-G. Park, Green solvent for perovskite solar cell production, Nat. Sustain. 4 (2021) 192–193, https://doi.org/10.1038/s41893-020-00647-6.
- [28] L. Zheng, L. Shen, T. Zhu, D. Zhang, J. Zheng, X. Gong, Stable and efficient perovskite solar cells by discrete two-dimensional perovskites capped on the threedimensional perovskites bilayer thin film, Nano Energy 96 (2022), 107126, https://doi.org/10.1016/j.nanoen.2022.107126.
- [29] C. Wu, K. Wang, J. Li, Z. Liang, J. Li, W. Li, L. Zhao, B. Chi, S. Wang, Volatile solution: the way toward scalable fabrication of perovskite solar cells? Matter 4 (2021) 775–793, https://doi.org/10.1016/j.matt.2020.12.025.
- [30] N.K. Noel, S.N. Habisreutinger, B. Wenger, M.T. Klug, M.T. Hörantner, M. B. Johnston, R.J. Nicholas, D.T. Moore, H.J. Snaith, A low viscosity, low boiling point, clean solvent system for the rapid crystallisation of highly specular perovskite films, Energy Environ. Sci. 10 (2017) 145–152, https://doi.org/10.1039/C6EE02373H.
- [31] D.-N. Jeong, D.-K. Lee, S. Seo, S.Y. Lim, Y. Zhang, H. Shin, H. Cheong, N.-G. Park, Perovskite cluster-containing solution for scalable D-bar coating toward highthroughput perovskite solar cells, ACS Energy Lett. 4 (2019) 1189–1195, https:// doi.org/10.1021/acsenergylett.9b00042.
- [32] Y.M. Xie, Q. Xue, H.L. Yip, Metal-halide perovskite crystallization kinetics: a review of experimental and theoretical studies, Adv. Energy Mater. 11 (2021), 2100784, https://doi.org/10.1002/aenm.202100784.
- [33] M. Saliba, T. Matsui, J.Y. Seo, K. Domanski, J.P. Correa-Baena, M.K. Nazeeruddin, S.M. Zakeeruddin, W. Tress, A. Abate, A. Hagfeldt, Cesium-containing triple cation perovskite solar cells: improved stability, reproducibility and high efficiency, Energy Environ. Sci. 9 (2016) 1989–1997, https://doi.org/10.1039/C5EE03874J.
 [34] T. Ozturk, E. Akman, A. Esmail Shalan, S. Akin, Composition engineering of
- [34] T. Ozturk, E. Akman, A. Esmail Shalan, S. Akin, Composition engineering of operationally stable CsPbI₂Br perovskite solar cells with a record efficiency over 17, Nano Energy 87 (2021), 106157, https://doi.org/10.1016/j. nanoen.2021.106157.
- [35] F. Qian, S. Yuan, Y. Cai, Y. Han, H. Zhao, J. Sun, Z. Liu, S. Liu, Novel surface passivation for stable FAO. 85MAO. 15Pbl3 perovskite solar cells with 21.6% efficiency, Solar RRL 3 (2019), 1900072, https://doi.org/10.1002/ solr.201900072.
- [36] X. Zhu, M. Du, J. Feng, H. Wang, Z. Xu, L. Wang, S. Zuo, C. Wang, Z. Wang, C. Zhang, High-efficiency perovskite solar cells with imidazolium-based ionic liquid for surface passivation and charge transport, Angew. Chem. Int. Ed. 60 (2021) 4238–4244, https://doi.org/10.1002/anie.202010987.
- [37] E. Jokar, C.H. Chien, A. Fathi, M. Rameez, Y.H. Chang, E.W.G. Diau, Slow surface passivation and crystal relaxation with additives to improve device performance and durability for tin-based perovskite solar cells, Energy Environ. Sci. 11 (2018) 2353–2362, https://doi.org/10.1039/C8EE00956B.
- [38] A. Mahapatra, D. Prochowicz, M.M. Tavakoli, S. Trivedi, P. Kumar, P. Yadav, A review of aspects of additive engineering in perovskite solar cells, J. Mater. Chem. 8 (2020) 27–54, https://doi.org/10.1039/C9TA07657C.
- [39] F. Zhang, K. Zhu, Additive engineering for efficient and stable perovskite solar cells, Adv. Energy Mater. 10 (2020), 1902579, https://doi.org/10.1002/ aeppp.201902579
- [40] C.C. Chueh, C.Y. Liao, F. Zuo, S.T. Williams, P.W. Liang, A.K.Y. Jen, The roles of alkyl halide additives in enhancing perovskite solar cell performance, J. Mater. Chem. 3 (2015) 9058–9062, https://doi.org/10.1039/C4TA05012F.
- [41] S. Liu, Y. Guan, Y. Sheng, Y. Hu, Y. Rong, A. Mei, H. Han, A review on additives for halide perovskite solar cells, Adv. Energy Mater. 10 (2020), 1902492, https://doi. org/10.1002/aenm.201902492.
- [42] D.P. McMeekin, Z. Wang, W. Rehman, F. Pulvirenti, J.B. Patel, N.K. Noel, M. B. Johnston, S.R. Marder, L.M. Herz, H.J. Snaith, Crystallization kinetics and morphology control of formamidinium–cesium mixed-cation lead mixed-halide perovskite via tunability of the colloidal precursor solution, Adv. Mater. 29 (2017), 1607039, https://doi.org/10.1002/adma.201607039.
- [43] M. Kim, G.H. Kim, T.K. Lee, I.W. Choi, H.W. Choi, Y. Jo, Y.J. Yoon, J.W. Kim, J. Lee, D. Huh, Methylammonium chloride induces intermediate phase stabilization for efficient perovskite solar cells, Joule 3 (2019) 2179–2192, https://doi.org/10.1016/j.joule.2019.06.014.

- [44] H. Zhang, Y. Lv, J. Wang, H. Ma, Z. Sun, W. Huang, Influence of Cl incorporation in perovskite precursor on the crystal growth and storage stability of perovskite solar cells, ACS Appl. Mater. Interfaces 11 (2019) 6022–6030, https://doi.org/10.1021/ acsami.8b19390.
- [45] F. Jiang, Y. Rong, H. Liu, T. Liu, L. Mao, W. Meng, F. Qin, Y. Jiang, B. Luo, S. Xiong, J. Tong, Y. Liu, Z. Li, H. Han, Y. Zhou, Synergistic effect of Pbl₂ passivation and chlorine inclusion yielding high open-circuit voltage exceeding 1.15 V in both mesoscopic and inverted planar CH₃NH₃Pbl₃ (CI)-Based perovskite solar cells, Adv. Funct. Mater. 26 (2016) 8119–8127, https://doi.org/10.1002/adfm.201603968.
- [46] L. Zheng, K. Wang, T. Zhu, Y. Yang, R. Chen, K. Gu, L. Chunming, X. Gong, High performance perovksite solar cells by one-step self-assembled perovskite-polymer thin films, ACS Appl. Energy Mater. 3 (2020) 5902–5912, https://doi.org/ 10.1021/acsaem.0c00823.
- [47] X. Zhang, L. Shen, P. Baral, S. Vijayaraghavan, F. Yan, X. Gong, H. Wang, Blade-coated inverted perovskite solar cells in an ambient environment, Sol. Energy Mater. Sol. Cells 246 (2022), 111894, https://doi.org/10.1016/j.solmat.2022.111894
- [48] L. Wang, C. McCleese, A. Kovalsky, Y. Zhao, C. Burda, Femtosecond time-resolved transient absorption spectroscopy of CH₃NH₃PbI₃ perovskite films: evidence for passivation effect of PbI₂, J. Am. Chem. Soc. 136 (2014) 12205–12208, https://doi. org/10.1021/ja504632z.
- [49] W.-C. Lin, W.-C. Lo, J.-X. Li, Y.-K. Wang, J.-F. Tang, Z.-Y. Fong, In situ XPS investigation of the X-ray-triggered decomposition of perovskites in ultrahigh vacuum condition, NPJ Mater. Degrad. 5 (2021) 13, https://doi.org/10.1038/s41529-021-00162-9.